J Mater Sci (2026) 61:11237–11249

Energy materials

CTAB–4,4′-bipyridine interface-mediated self-assembly of gold nanobipyramids into stable plasmonic chains

Lan Chen[1], Xi-Hao Zhang[1], Hironori Ito[2], and Tian-Song Deng[1,*]

[1] School of Electronics and Information Engineering, Hangzhou Dianzi University, Hangzhou 310018, People's Republic of China
[2] Integrated Graduate School of Medicine, Engineering, and Agricultural Sciences, University of Yamanashi, 4-3-11, Takeda, Kofu, Yamanashi 400-8510, Japan

Received: 12 December 2025
Accepted: 26 February 2026
Published online: 9 March 2026

ABSTRACT

Gold nanobipyramids (AuNBPs) possess sharp tips and highly tunable near-infrared localized surface plasmon resonance (LSPR) modes, making them attractive building blocks for plasmonic superstructures. However, achieving controllable and stable one-dimensional (1D) self-assembly in aqueous phase remains challenging. Here, we present an interface-mediated strategy in which CTAB regulates tip accessibility, while 4,4′-bipyridine (4,4′-BPy) participates in coordination-assisted interactions that modulate the assembly pathway and bias AuNBPs toward end-to-end configurations. Controlled CTAB desorption selectively exposes the {111} tip sites, enabling ligand-assisted interactions that favor anisotropic chain growth. Subsequent CTAB re-passivation enables kinetic stabilization of the assemblies, allowing chain elongation to be terminated at selected stages and yielding plasmonic nanochains with good long-term structural stability. Together, this synergistic combination of interfacial regulation, coordination-assisted interactions, and kinetic stabilization provides a versatile framework for constructing stable near-infrared plasmonic architectures and offers general design principles for manipulating collective optical modes in anisotropic nanostructure assemblies.

Introduction

Self-assembled superstructures of metal nanoparticles have emerged as a frontier research direction in nanotechnology due to their capability to manipulate optical, electrical, and magnetic properties at subwavelength scales [1, 2]. Such superstructures show tremendous potential in nanophotonics [3], sensing [4, 5], catalysis [6, 7], and biomedicine [8, 9]. Among various nanoscale building blocks, anisotropic gold nanorods (AuNRs) and gold nanobipyramids (AuNBPs) are considered ideal materials for constructing

Handling Editor: Ivo Teixeira.

Address correspondence to E-mail: dengts@pku.edu.cn

https://doi.org/10.1007/s10853-026-12527-z

functional plasmonic superstructures owing to their morphology-dependent localized surface plasmon resonance (LSPR) characteristics and high spectral tunability [10–12].

1D chain-like structures have attracted considerable attention because they can delocalize collective plasmonic modes along the chain axis through strong near-field coupling between nanoparticles [13]. This coupling effect can efficiently redshift the LSPR peak into the near-infrared region and generate intense local electric field enhancement at particle gaps (i.e., "hot spots") [14], which is crucial for applications in plasmonic waveguides [15], surface-enhanced Raman scattering (SERS) detection [16], and photothermal therapy [17].

Achieving end-to-end directional assembly of anisotropic nanoparticles represents a core challenge in constructing ordered 1D superstructures, even in light of recent advances in the controlled self-assembly of shape-anisotropic gold nanocrystals into diverse superstructures [18–20]. Current assembly strategies include coordination chemistry [21–25], template-guided methods [26], polymer region-selective adsorption [27], and external electric field induction [28–31]. However, many existing approaches either rely on complex surface functionalization steps [32] or are limited to non-aqueous systems [33], restricting their universality. Moreover, precise control of assembly kinetics and ensuring long-term structural stability of assemblies in aqueous environments remain critical issues in this field [34].

Recently, competitive adsorption strategies based on surfactants and functional ligands have provided new insights for addressing these challenges [35]. This approach enables facet-selective assembly through fine interfacial chemistry modulation [36]. For instance, linear chromophores such as BODIPY derivatives have been used to specifically bind AuNRs tips, inducing stable end-to-end assembly and imparting excellent photothermal properties [37]. Additionally, controlling self-assembly of silica-coated nanocrystal networks through ligand-depletion-induced gelation can yield structurally stable assemblies [38].

Although 1D assembly of AuNRs has been well established, AuNBPs offer unique advantages for plasmonic applications [39]. AuNBPs possess sharper tips, stronger electromagnetic field enhancement capability, and narrower LSPR linewidth [40], demonstrating great potential in constructing macroscopic superlattices [41] and photothermal conversion [42]. However, AuNBPs are typically stabilized by cetyltrimethylammonium bromide (CTAB), and their highly reactive {111} facets at the tips, while facilitating reactions, also lead to poor colloidal stability [43]. This inherent instability makes controllable, terminable, and long-term stable 1D self-assembly of AuNBPs in aqueous phase extremely challenging, hindering the full exploitation of their superior optical properties.

In this study, we propose a synergistic strategy utilizing CTAB-regulated interfacial accessibility together with coordination-assisted interactions involving 4,4′-bipyridine (4,4′-BPy) to bias the assembly toward end-to-end chain formation. By precisely regulating CTAB concentration, the accessibility of AuNBPs tips is modulated, allowing 4,4′-BPy to participate in pathway-selective assembly rather than acting as a sole driving linker. Using time-resolved spectroscopy, TEM tracking, and finite difference time domain (FDTD) simulations, we elucidate the kinetic pathway and the emergence of collective plasmonic coupling during chain formation. A central advance of this work is the introduction of a CTAB re-passivation step that enables kinetic stabilization of the assemblies, allowing the assembly process to be actively terminated at selected stages while preserving the resulting chain structures. This integrated framework provides a versatile and generalizable route for constructing stable near-infrared plasmonic architectures through interfacial regulation, coordination-assisted interactions, and kinetic stabilization.

Results and discussion

Self-assembly of gold nanobipyramids

Gold nanobipyramids (AuNBPs) exhibit remarkable electromagnetic enhancement effects due to their high-curvature tip structures, offering unique advantages in plasmonic coupling studies. Compared to blunt-ended gold nanorods, AuNBPs possess sharper tips, stronger electric field confinement, higher refractive index sensitivity, and narrower bandwidth of LSPR. These features enable tunable LSPR modes in the 600–1100 nm range. The AuNBPs synthesized via seed-mediated growth in this study show uniform morphology with average dimensions of 90.3 ± 4.5 nm in length and 30.1 ± 1.8 nm in width, displaying a characteristic LSPR peak at 777 nm (Fig. S1).

The overall experimental strategy for assembling AuNBPs into one-dimensional structures is illustrated in Fig. 1. In a typical procedure, CTAB-stabilized AuNBPs were mixed with 4,4′-BPy at controlled concentrations to trigger directional particle association in aqueous solution. Upon introduction of 4,4′-BPy, the pyridyl groups can interact with accessible gold sites near the AuNBPs tips through coordination-assisted interactions, thereby biasing particle association toward end-to-end configurations. The assembly was allowed to proceed for predefined time intervals so that intermediate structures at different stages could be captured. By quenching the reaction at selected time points, we monitored the structural evolution from isolated AuNBPs to tip-linked dimers and subsequently elongated chains. Following this time-dependent assembly workflow, the resulting architectures were examined by TEM to visualize their morphological progression throughout the assembly process.

To elucidate the assembly kinetics, the time-dependent evolution of AuNBPs chains under reference standard conditions (CTAB 10 μM, 4,4′-BPy 1 mM) was systematically monitored using a rapid quenching–silica encapsulation protocol, ensuring faithful preservation of transient intermediates. Time-resolved TEM imaging combined with quantitative particle statistics (Figs. 2a–b and S2) reveals a well-defined assembly progression. At 0 min, the dispersion contains predominantly monodisperse AuNBPs, with the monomer fraction exceeding 85% (Fig. S2a). After 5 min, the monomer population decreases markedly and dimers become the major species (~ 45%), accompanied by the appearance of a small number of trimers (Fig. S2b), confirming the onset of 4,4′-BPy–mediated tip coordination. By 15 min, medium-length chains emerge as the dominant intermediates, and the multimer fraction surpasses that of dimers (Figs. 2a and S2c), signaling a transition into a rapid chain-growth regime. At 30 min, extended chains comprising several AuNBPs dominate the system (Fig. S3), with multimer fractions above 70% and chain length approaching saturation (Fig. S2d). This continuous shift from monomers to progressively longer assemblies reflects a stepwise polymerization-like kinetic behavior.

Higher-magnification TEM imaging (Fig. 2c–h) reveals that the resulting structures deviate from an idealized, perfectly linear "tip-to-tip" geometry. Instead, AuNBPs consistently adopt a subtly "staggered end-to-end stacking" configuration characterized by a slight lateral displacement between neighboring particles. Such an arrangement emerges from the interplay of ligand accessibility, steric modulation, and interparticle energetics. The highly curved AuNBPs tips provide preferred sites for 4,4′-BPy coordination, yet the minimal effective contact area at the very apex makes a perfectly axial connection less favorable. A slight offset helps relieve steric congestion originating from CTAB molecules residing near the tip regions, while the dynamic adsorption behavior of CTAB occasionally exposes coordination-permissive sites on facets adjacent to the tips. At the same time, the staggered geometry enhances van

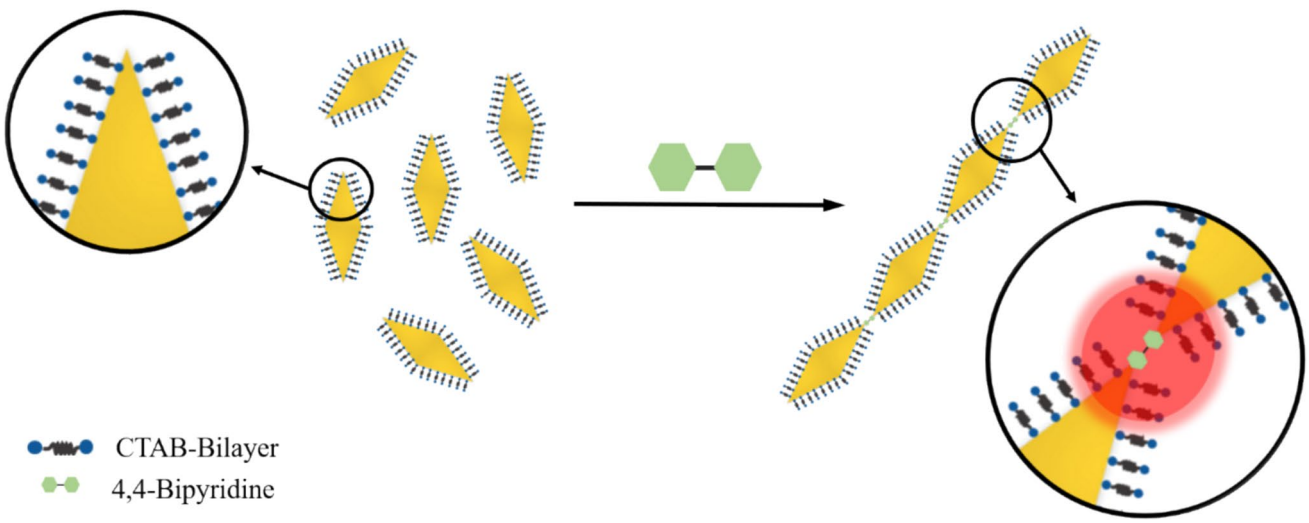

Figure 1 Schematic illustration of CTAB-regulated, coordination-assisted one-dimensional assembly of AuNBPs mediated by 4,4′-BPy.

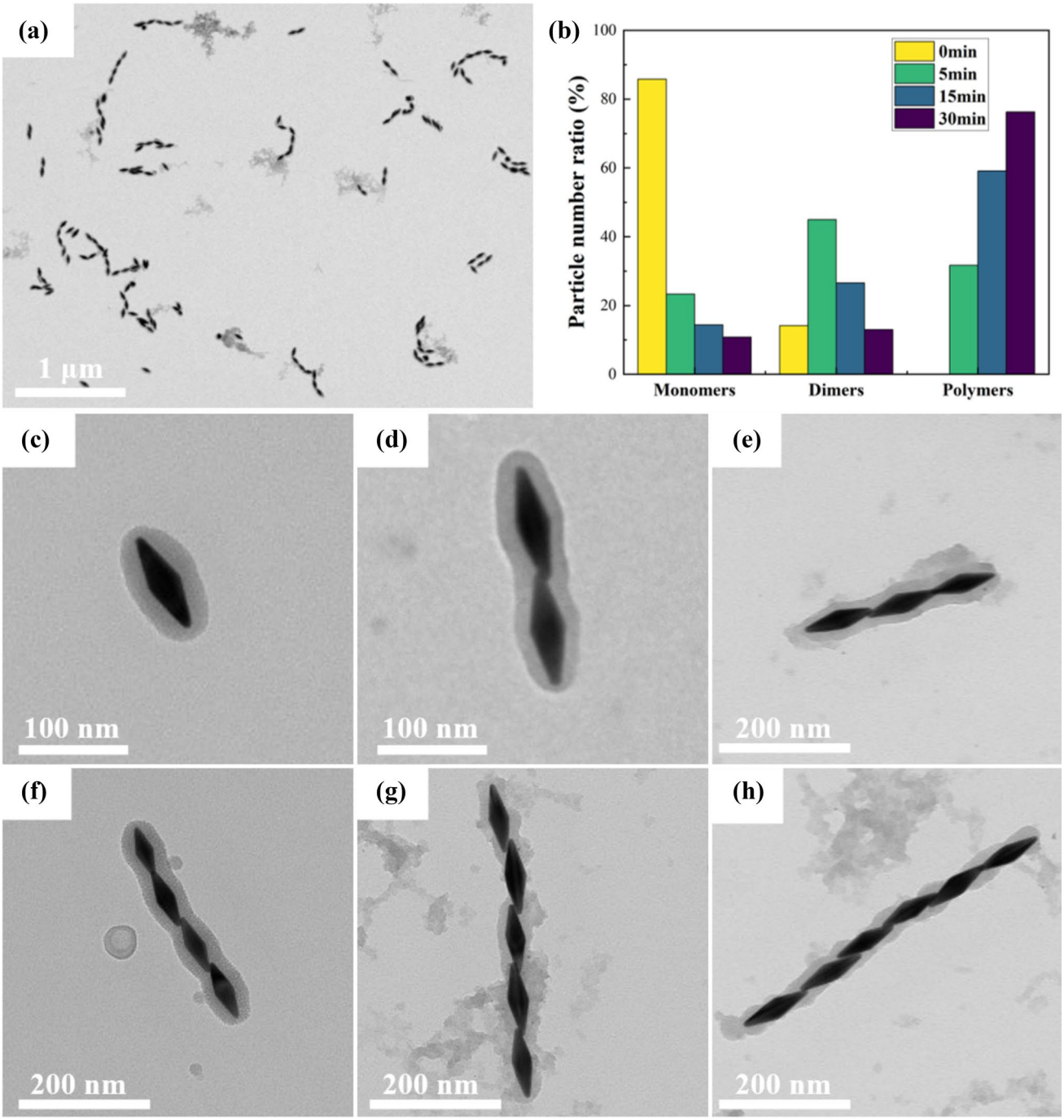

Figure 2 **a** TEM image of AuNBPs after 15 min assembly under CTAB (10 μM) and 4,4′-BPy (1 mM) conditions, followed by SiO_2 coating; **b** Percentage statistics of monomers, dimers, and multimers at different assembly times (0, 5, 15, 30 min); and **c**–**h** TEM images of SiO_2-coated linear structures from monomer to hexamer.

der Waals interactions by enlarging the interparticle contact area without compromising Au–N coordination. As these effects converge, the assembly evolves toward a configuration dominated by directional tip coordination but subtly adjusted by steric and energetic considerations. The resulting chain-like architectures thus embody a kinetically accessible balance between directional interactions and configurational

flexibility. Taken together, the coexistence of finite interparticle gaps and near-contact configurations observed in Fig. S3 suggests that the assembly is governed by multiple concurrent interactions.

Time-dependent study: CTAB–4,4′-BPy system

Building upon morphological analyses, in situ time-resolved UV–Vis–NIR spectroscopy was employed to track the optical signatures and kinetic behavior of AuNBPs chain formation in the CTAB–4,4′-BPy system.

The spectral evolution under reference standard conditions (Fig. 3a) closely parallels the structural development revealed by TEM. In the early period (0–5 min), the longitudinal LSPR peak of isolated AuNBPs at 777 nm undergoes a slight redshift accompanied by a decrease in intensity, indicating the formation of plasmonically coupled dimers, consistent with the early intermediates observed in Fig. S2b. As the reaction proceeds (5–15 min), a broad absorption feature emerges and intensifies in the 800–1100 nm range. This newly developed band corresponds to longitudinal collective plasmonic modes associated with multi-particle end-to-end coupling, matching the appearance of medium-length chains at 15 min (Fig. S2c). At later times (15–40 min), absorption beyond 1000 nm continues to increase and gradually levels off, reflecting the saturation of chain extension and the dominance of long-chain structures at 30 min (Fig. S2d). To further verify that the optical signatures are preserved during the quenching process, assemblies arrested at different time points by CTAB addition were subsequently encapsulated with silica. As shown in Fig. S4, the extinction spectra recorded before and after silica encapsulation exhibit a uniform redshift of the longitudinal LSPR peak without noticeable peak broadening or line shape distortion, indicating that the underlying one-dimensional assembly structures are preserved.

It should be noted that the spectral evolution observed during the assembly process does not correspond to a simple redshift of a single longitudinal plasmon mode. Instead, the extinction spectra reflect an ensemble-averaged response from coexisting AuNBPs monomers, dimers, and chains with different lengths and non-ideal geometries. As assembly proceeds, the depletion of isolated AuNBPs leads to an apparent damping of the original longitudinal LSPR peak at ~ 777 nm, while a broad near-infrared band gradually develops due to collective plasmonic coupling in multi-particle chains. Moreover, the slight lateral offsets and staggered end-to-end configurations frequently observed in TEM images further broaden the plasmonic response and suppress the emergence of a single sharp resonance. Consequently, the optical signature of the system manifests as a redistribution of spectral intensity toward longer wavelengths rather than a distinct peak shift, which is commonly observed in ensemble plasmonic coupling of anisotropic nanoparticle assemblies.

To quantify assembly kinetics, the decay of the monomeric LSPR at 777 nm was monitored, and $-\ln(A_t/A_0)$ was plotted as a function of time to extract the initial linear regime. The resulting slope k was taken as the apparent assembly rate constant (Figs. 3b–c and S5–S6).

CTAB concentration strongly modulates the kinetic behavior (Fig. 3b). When CTAB exceeds 12 μM, the

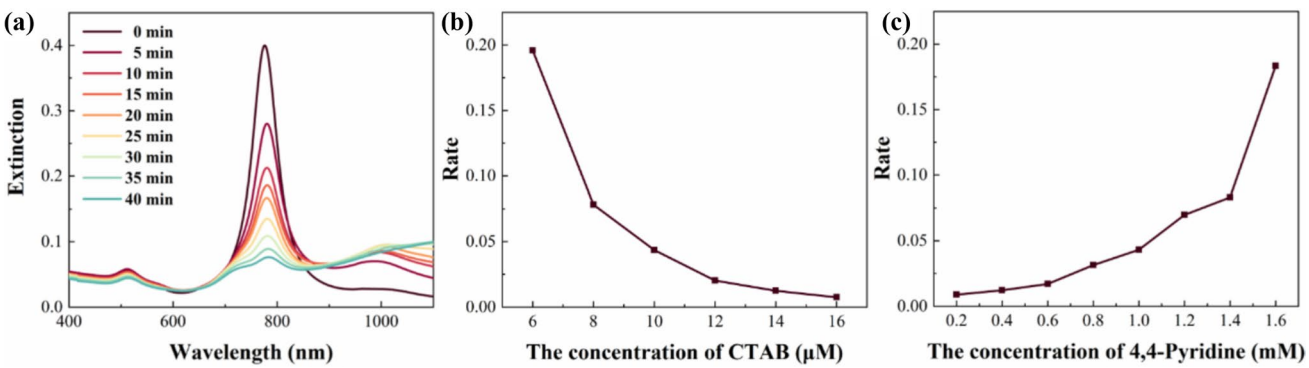

Figure 3 **a** Time-evolution of extinction spectra of assembly solution under CTAB (10 μM) and 4,4′-BPy (1 mM); **b** Comparison of assembly rates at different CTAB concentrations with fixed 4,4′-BPy (1 mM); and **c** Comparison of assembly rates at different 4,4′-BPy concentrations with fixed CTAB (10 μM).

spectra remain nearly unchanged, indicating that densely packed CTAB bilayers significantly suppress chain formation by limiting the accessibility of sites that are favorable for coordination near the tip regions. As CTAB decreases to 8–10 μM, mild redshift and weak coupling features appear, suggesting partial ligand desorption and gradual exposure of tip sites. Further reduction to 6–8 μM markedly accelerates assembly, leading to rapid intensification of the near-infrared coupling band. These trends illustrate the regulatory role of CTAB in controlling the accessibility of coordination sites.

The influence of 4,4′-BPy concentration is similarly pronounced (Fig. 3c). Under fixed CTAB (10 μM), increasing 4,4′-BPy from 0.2 to 1.6 mM progressively enhances assembly rates. At low 4,4′-BPy levels (≤ 0.4 mM), coordination-assisted interactions are insufficient to promote pronounced plasmonic coupling, resulting in weak near-infrared features. Moderate concentrations (0.6–1.0 mM) efficiently activate chain growth and yield rapid development of the collective plasmonic band. At higher concentrations, the coupling band broadens and reaches saturation more rapidly due to accelerated assembly kinetics; as the assembly approaches saturation, the overall extinction intensity decreases, reflecting enhanced aggregation.

Self-assembly mechanism

As illustrated in Fig. 4, the self-assembly of AuNBPs is governed by a local and kinetic form of competitive adsorption between CTAB and 4,4′-BPy at surface sites with different local geometries. In CTAB-stabilized systems, the {100}/{110} side facets are densely passivated by interdigitated CTAB chains. The {111} tips, owing to their high curvature, remain the most accessible regions for ligand-mediated interactions, as the local packing density of surfactant molecules is reduced at these sites [44]. Under CTAB-rich conditions (upper pathway in Fig. 4), a complete CTAB bilayer forms over the entire surface, including full tip passivation. This steric barrier prevents ligand access to the gold surface, thereby suppressing ligand-mediated adsorption or coordination-assisted interactions and maintaining a monodisperse dispersion. Accordingly, no plasmon-coupling features appear in the near-infrared region, consistent with the absence of tip-to-tip interactions.

When the CTAB concentration becomes insufficient to maintain full tip coverage (lower pathway in Fig. 4), adsorption equilibrium shifts and partial desorption occur preferentially at the {111} tips, placing the AuNBPs dispersion into a metastable regime [34] that permits kinetically accessible particle association. The exposed sites can be transiently accessed by adsorbed 4,4′-BPy, whose bidentate structure enables weak, orientation-dependent coordination or adsorption interactions between adjacent AuNBPs [45] and biases the assembly pathway toward end-to-end configurations, without excluding nonlinear association pathways. Importantly, under these controlled CTAB conditions, the lateral {100}/{110} facets remain largely

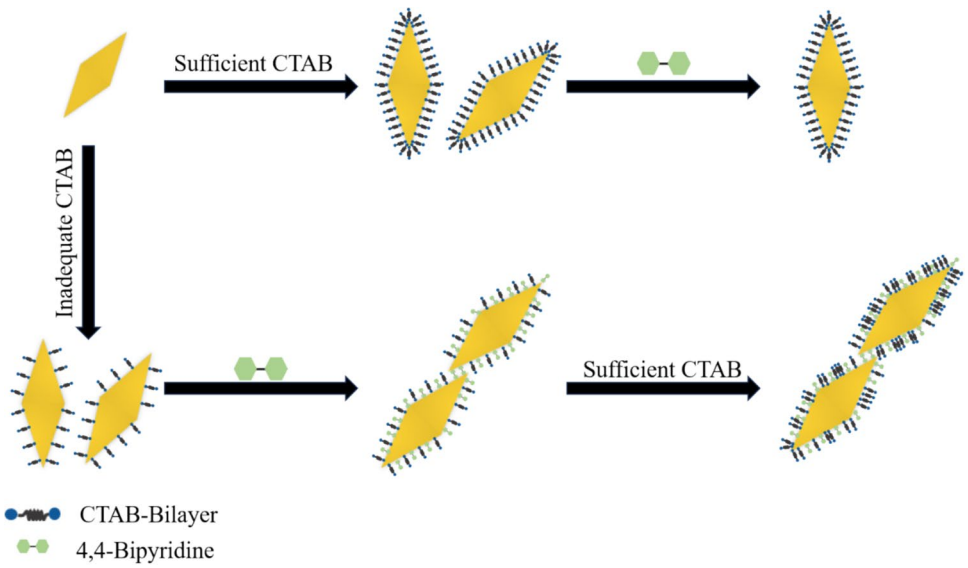

Figure 4 Schematic illustration of CTAB–4,4′-BPy co-regulated assembly pathways of AuNBPs.

passivated, which suppresses extensive side-to-side association despite the presence of 4,4′-BPy. Previous spectroscopic studies on pyridine adsorption at Au surfaces have shown that nitrogen lone-pair donation can give rise to σ-type Au–N coordination under suitable interfacial conditions [46]; in the present colloidal system, however, such coordination is expected to be localized, reversible, and dynamically regulated by surfactant coverage and interparticle geometry, rather than forming a rigid or permanent molecular bridge. Accordingly, Fig. 4 schematically illustrates a coordination-assisted interaction motif at accessible tip regions, rather than a fixed bonding configuration. Within this metastable regime, CTAB depletion provides a necessary background condition for particle association, whereas 4,4′-BPy regulates the assembly pathway and kinetics under a given CTAB concentration. The dependence of assembly rate, chain length evolution, and final morphology on the 4,4′-BPy concentration cannot be explained by CTAB depletion alone, indicating the cooperative involvement of electrostatic interactions, van der Waals attraction, surfactant reorganization, and localized, reversible coordination-assisted interactions. The assembled chains frequently exhibit finite interparticle gaps and slight lateral offsets in TEM images, reflecting the dynamic and non-ideal nature of the assembly process governed by competing interfacial interactions.

After chains form, reintroduction of excess CTAB rapidly reconstructs the dense bilayer around each particle, blocking further ligand-mediated association and effectively arresting further chain growth in a kinetically stabilized state. Stability tests (Fig. S7) show that although minor blueshifts and intensity decreases are observed over one month, no progressive spectral evolution or features indicative of further assembly or structural reorganization occur. The SERS measurements (Fig. S8) further indicated the involvement of 4,4′-BPy in the interfacial processes accompanying assembly, as only the assembled samples exhibited clear bipyridine vibrational signatures (e.g., 1015, 1297, and 1610 cm^{-1}). The appearance of these characteristic bands indicates that 4,4′-BPy participates in the interfacial processes accompanying assembly and plays a role in regulating nanoparticle association.

FDTD simulation of plasmonic chains

To investigate the plasmonic coupling behavior of AuNBPs assemblies, FDTD simulations were performed using geometric parameters obtained from TEM analysis. Individual particles were modeled as back-to-back bicones, and two representative classes of superstructures were constructed to capture the dominant coupling motifs observed experimentally. The first class involved linear chains with controlled bending, where chain lengths were set to $n = 1–6$ and bending angles adjusted to 0°, 30°, 60°, 90°, and 120°, as shown in Figs. 5 and S9–S12. These models were used to establish the intrinsic dependence of longitudinal plasmon coupling on chain length and bending geometry. The second class involved laterally staggered or partially overlapped chains. In Fig. 6, the overlap degree was fixed at 11.11% with chain lengths of $n = 2–5$, while simulations with higher overlap degrees of 50% and 100% are presented in Figs. S13

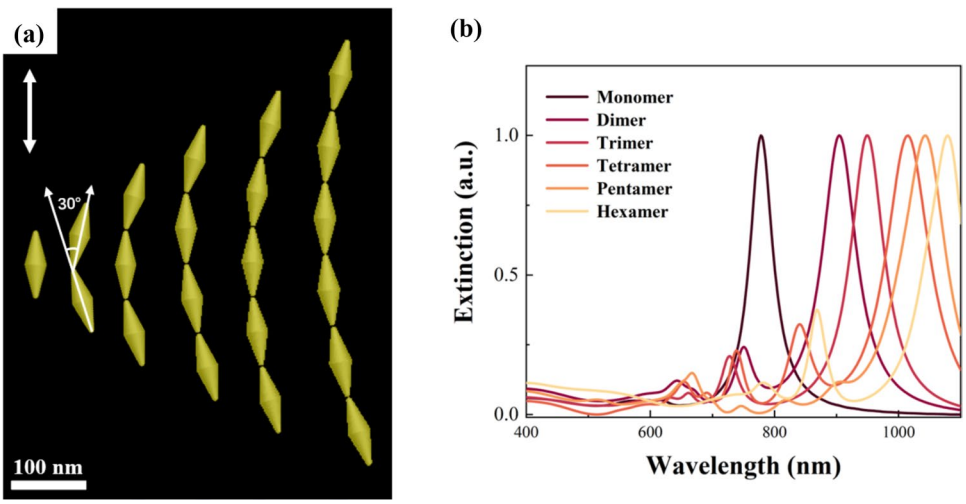

Figure 5 **a** Geometric models and **b** corresponding FDTD-simulated extinction spectra of AuNBPs assemblies with different chain lengths ($n = 1–6$) at a bending angle of 30°.

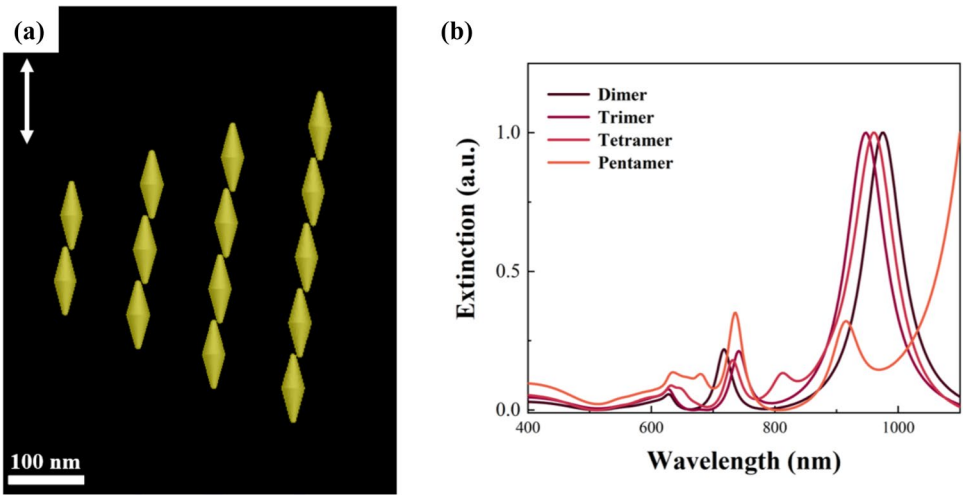

Figure 6 **a** Geometric models and **b** corresponding FDTD-simulated extinction spectra of AuNBPs assemblies with different chain lengths ($n = 2$–5) at 11.11% lateral overlap.

and S14. These configurations were introduced to represent the structural variability frequently observed in TEM images and to examine how lateral misalignment modifies the plasmonic response. For all configurations, the interparticle spacing was fixed at 1 nm as a representative nanoscale separation, consistent with experimentally observed interparticle spacings. Illumination was polarized along the particle long axis, matching the excitation configuration in Fig. 5a.

The simulations of linear end-to-end chains establish a baseline for understanding the intrinsic plasmonic coupling behavior of AuNBPs assemblies. As qualitatively depicted in Fig. 5b, the longitudinal LSPR exhibits a monotonic dependence on chain length and undergoes a continuous redshift as additional particles are incorporated. This trend reflects the gradual extension of the near-field coupling pathway and the increasing hybridization of plasmon modes along the chain axis, which together give rise to more delocalized collective oscillations. The results in Figs. S9–S12 further indicate that this chain length-dependent redshift is preserved across a series of discretely defined bending angles (0°, 30°, 60°, 90°, and 120°), demonstrating that chain length remains the primary determinant of the plasmonic response in these linear configurations. Accordingly, these linear-chain simulations serve as a reference framework against which more structurally complex and experimentally relevant assemblies can be compared.

In addition to idealized linear chains, the experimentally observed AuNBPs assemblies frequently exhibit laterally staggered and partially overlapped configurations, as illustrated by the representative models and simulated extinction spectra shown in Fig. 6, which constitute a second representative class of plasmonic coupling geometries. In Fig. 6, the lateral overlap between adjacent AuNBPs is fixed at 11.11%, while the chain length is varied from $n = 2$–5, allowing the influence of chain length on plasmonic coupling to be examined under a representative staggered configuration. Although the simulated extinction spectra are normalized, comparison of peak positions indicates that most staggered configurations exhibit coupling-induced spectral shifts toward lower energies compared with the single-particle response, reflecting enhanced plasmonic hybridization. However, the precise peak locations depend sensitively on the overlap extent and local arrangement of adjacent particles, and the resulting extinction spectra do not follow a simple monotonic progression with increasing chain length. At a moderate overlap degree (50% overlap, Fig. S13), the staggered chains generally exhibit a systematic redshift relative to isolated particles, consistent with strengthened interparticle coupling, while the resonance peaks remain relatively well defined and do not show pronounced spectral broadening. In contrast, for highly overlapped configurations (100% overlap, Fig. S14), lateral coupling can dominate over longitudinal interactions, leading to non-monotonic spectral evolution and, in some cases, blueshifted resonances, accompanied by increased mode competition.

The simulation results underscore that the experimental spectra cannot be quantitatively reproduced by any single structural model. In the assembly solutions, a distribution of chain lengths inevitably coexists with multiple non-ideal geometries, whose relative

populations are not experimentally accessible. Consequently, the measured near-infrared response represents an ensemble-averaged spectrum arising from many coexisting configurations. The chain length dependence illustrated in Fig. 5, together with the representative staggered-chain simulations shown in Fig. 6 and the broader set of simulated geometries provided in Figs. S9–S14, supports the interpretation that the experimentally observed near-infrared band broadening originates from the superposition of plasmonic modes associated with chains of different lengths and varying degrees of misalignment. Accordingly, the FDTD results are intended to elucidate plasmonic coupling trends for representative chain geometries, rather than to quantitatively reproduce the ensemble-averaged experimental spectra.

Conclusions

In summary, we have constructed an aqueous assembly system for AuNBPs regulated by CTAB-modulated interfacial barriers together with coordination-assisted interactions involving 4,4′-BPy that bias particle association toward end-to-end configurations, achieving controllable, terminable, and structurally stable self-assembly of AuNBPs chain structures. Through combined time-resolved TEM and in situ spectroscopic analysis, we have clarified the complete kinetic pathway of AuNBPs from tip activation, dimer formation, rapid chain elongation to chain length saturation. Results indicate that local CTAB desorption is the crucial step for exposing coordination-accessible sites, while the bipyridine structure of 4,4′-BPy modulates the assembly pathway and kinetics rather than acting as a single dominant chemical driving force for 1D chain construction. FDTD simulations further reveal that the chain length-dependent longitudinal plasmonic and geometry-dependent coupling behavior are consistent with experimental spectra, with bent segments and laterally misaligned chains also exhibiting distinct optical coupling behavior. In addition, reintroduction of CTAB at high concentration enables kinetic stabilization of the assembled structures at selected time points, yielding chain morphologies with excellent long-term stability that largely maintain their overall spectral characteristics at room temperature. SERS measurements provide spectroscopic evidence for the participation of ligand-assisted and coordination-mediated interactions during assembly. These results collectively establish a clear self-assembly framework: Interfacial adsorption regulation determines tip accessibility, coordination-assisted interactions guide pathway-selective chain growth, and subsequent CTAB re-passivation enables kinetic stabilization of the assemblies. This study not only deepens the understanding of AuNBPs interfacial chemistry and self-assembly mechanisms but also provides a generalizable framework for constructing stable near-infrared plasmonic chain structures, laying a solid foundation for future exploration of applications in nanophotonics, photothermal effects, SERS, and field-enhanced catalysis.

Experimental section

Materials

All chemicals were of analytical grade and used without further purification. Cetyltrimethylammonium bromide (CTAB, > 99.0%), L-ascorbic acid (AA, > 99.99%), chloroauric acid ($HAuCl_4$), hydrochloric acid (37.0 wt% aqueous solution), and 4,4′-bipyridine (4,4′-BPy) (≥ 98.0%) were purchased from Macklin; cetyltrimethylammonium chloride (CTAC, > 99.0%), sodium borohydride ($NaBH_4$, ≥ 98.0%), sodium citrate dihydrate (SC, ≥ 99.0%), silver nitrate ($AgNO_3$, > 99.8%), and benzyldimethylhexadecylammonium chloride (HDBAC, ≥ 95.0%) were obtained from Aladdin. Ultrapure water (18.2 MΩ·cm, Milli-Q system) was used throughout all experiments. All glassware for AuNBPs synthesis was cleaned with freshly prepared aqua regia (HCl/HNO_3, 3:1 v/v), rinsed thoroughly with ultrapure water, and dried at 60 °C prior to use.

Synthesis of gold nanobipyramids

AuNBPs were synthesized using a seed-mediated growth method. Briefly, an ice-cold $NaBH_4$ solution (0.025 M, 0.25 mL) was rapidly injected into a mixture of $HAuCl_4$ (0.01 M, 0.25 mL), sodium citrate (0.01 M, 5.0 mL), and CTAC (0.1 M, 5.0 mL) under vigorous stirring, followed by continuous stirring for 2 min to form gold seeds. The seed solution was then transferred to an 80 °C water bath and slowly stirred for 90 min, during which the solution color gradually changed from brown to red, indicating seed formation. Subsequently, the seed solution (0.1 mL) was added to a

growth solution (composition: CTAB 0.1 M, 20.0 mL; $HAuCl_4$ 0.01 M, 1.0 mL; $AgNO_3$ 0.01 M, 0.2 mL; HCl 1.0 M, 0.4 mL; and AA 0.1 M, 0.16 mL), gently mixed by inversion for 10 s, and left undisturbed at 30 °C overnight to complete AuNBPs growth.

The as-synthesized AuNBPs were purified via a two-step centrifugation process to remove byproducts and unreacted precursors. The reaction mixture was first centrifuged at 9000 rpm for 10 min, the supernatant was discarded, and the pellet was redispersed in CTAB solution (1.5 mM, 6.0 mL). Then, HDBAC solution (0.5 M, 14.0 mL) was added and incubated at 30 °C for 24 h to selectively precipitate AuNBPs. After removing the purple supernatant, CTAB solution (1.5 mM, 5.0 mL) was added, and the particles were resuspended by sonication for 1 min. This purification procedure was repeated twice to completely remove residual HDBAC. Finally, the purified AuNBPs were dispersed in CTAB solution (1.5 mM, 1.0 mL) and stored at 4 °C in the dark.

1D chain-like self-assembly of AuNBPs

For a typical assembly experiment, a defined volume of 4,4′-BPy solution (5.0 mM) and a CTAB solution were mixed with deionized water to give a total volume of 2.0 mL. Depending on the target final CTAB concentration, CTAB stock solutions with different concentrations (10.0 μM or 0.5 mM) were used. Subsequently, 8.0 μL of the AuNBPs stock dispersion (stabilized in 1.5 mM CTAB) was added, and the contribution of residual CTAB from the AuNBPs stock was included when calculating the overall CTAB concentration after mixing. The reaction proceeded at room temperature under gentle stirring (300 rpm). At the selected time point, 2.0 mL of 3.0 mM CTAB solution was introduced to re-passivate the particle surfaces, thereby suppressing further ligand-mediated association and kinetically stabilizing the assembly state.

The effective concentration of AuNBPs in the assembly solution was estimated from the UV–Vis–NIR extinction spectrum rather than from the initial gold precursor concentration, due to particle loss during synthesis and purification. The initial longitudinal LSPR peak intensity of the dispersion was approximately OD ≈ 0.4 at ~ 777 nm (optical path length = 1 cm). Following established treatments that relate the extinction cross section of anisotropic gold nanostructures to optical density [47], the particle concentration was estimated to be on the order of ~ 0.05 nM.

Silica coating of assemblies

To facilitate reliable observation of the solution-assembled structures after kinetic stabilization by excess CTAB, AuNBPs assemblies were subsequently coated with SiO_2 as a post-assembly treatment. Briefly, 4 mL of assembly solution was stirred at 800 rpm, and NaOH solution (0.1 M, 0.04 mL) and TEOS methanol solution (12.0 μL, 20 vol%) were sequentially added. Additional equal aliquots of TEOS solution were added at 1 h intervals, repeated twice. After continuous stirring for 24 h, the solution was centrifuged at 9000 rpm for 10 min and washed twice each with water and methanol. The final SiO_2-coated AuNBPs assemblies were dispersed in 1 mL methanol.

Characterization

Extinction spectra were recorded using a Shimadzu UV-1900i spectrophotometer with a 10 mm path length over the range of 400–1100 nm. TEM images were acquired on a Hitachi HT-7700 transmission electron microscope at an acceleration voltage of 100 kV. Particle size and assembly statistics were performed using ImageJ software, with at least 100 particles counted per sample to ensure statistical significance.

SERS performance testing of assemblies

SERS measurements were conducted using a Horiba LabRAM HR Evolution confocal Raman spectrometer. Silicon substrates were cleaned sequentially by sonication in acetone and ethanol and then dried. For experimental groups, 10 μL of AuNBPs solution (containing 10 μM CTAB and 1 mM 4,4′-BPy) assembled for 15 min was drop-cast onto the substrate, while control groups received an equal volume of 1 mM 4,4′-BPy solution. Measurements were performed after air-drying using the following parameters: 50 × objective, ~ 1 μm laser spot diameter, 1% laser power, 10 s integration time, 150 g/mm grating, single acquisition.

FDTD simulations

The FDTD method is an explicit time-marching algorithm used to solve Maxwell's curl equations on a discretized spatial grid. The FDTD simulations were

carried out with a commercial software, FDTD Solutions (Lumerical, Ansys). A light pulse in the wavelength range of 400–1100 nm was launched into a simulation domain (box) containing AuNBPs assemblies to simulate a propagating plane light wave interacting with the nanostructures. The structures were surrounded by a virtual boundary (Perfectly Matched Layer, PML) with an appropriate size. A non-uniform mesh was applied, with the interparticle gap regions refined to 2 nm and other areas set to a lower density. The sizes of the AuNBPs were taken from their average values and constructed using a bicone geometry. The refractive indices of the surrounding air and water were set to be 1.00 and 1.33, respectively.

Acknowledgements

The authors thank Sudan Shen for her assistance in TEM at State Key Laboratory of Chemical Engineering (Zhejiang University). T.S.D. acknowledges financial support from Zhejiang Provincial Natural Science Foundation (Grant: LY24F050008) and National Natural Science Foundation of China (NSFC, Grant: 61905056).

Author contributions

All authors contributed to the conception and design of the study. Tian-Song Deng performed supervision, funding acquisition, and writing—review and editing. Lan Chen was responsible for investigation, writing—original draft, and visualization. Xi-Hao Zhang conducted investigation. Hironori Ito contributed to writing—review and editing.

Data availability

The data that support the findings of this study are available from the corresponding author upon reasonable request.

Declarations

Conflict of interest The authors declare no conflict of interest.

Supplementary Information The online version contains supplementary material available at https://doi.org/10.1007/s10853-026-12527-z.

References

[1] Lee MS, Yee DW, Ye M, Macfarlane RJ (2022) Nanoparticle assembly as a materials development tool. J Am Chem Soc 144:3330–3346

[2] Boles MA, Engel M, Talapin DV (2016) Self-assembly of colloidal nanocrystals: from intricate structures to functional materials. Chem Rev 116:11220–11289

[3] Ghosh SK, Pal T (2007) Interparticle coupling effect on the surface Plasmon resonance of Gold nanoparticles: from theory to applications. Chem Rev 107:4797–4862

[4] Amestoy A, Rangra A, Mansard V, Saya D, Pouget E, Mazaleyrat E, Severac F, Bergaud C, Oda R, Delville M-H (2023) Highly stable low-strain flexible sensors based on Gold nanoparticles/Silica nanohelices. ACS Appl Mater Interfaces 15:39480–39493

[5] Han X, Liu Y, Yin Y (2014) Colorimetric stress memory sensor based on disassembly of Gold nanoparticle chains. Nano Lett 14:2466–2470

[6] Gao J, Wu WB, Lemaire V, Carvalho A, Nlate S, Buffeteau T, Oda R, Battie Y, Pauly M, Pouget E (2020) Tuning the chiroptical properties of elongated nano-objects via hierarchical organization. ACS Nano 14:4111–4121

[7] Fu J, Zhu W, Chen Y, Yin Z, Li Y, Liu J, Zhang H, Zhu J-J, Sun S (2019) Bipyridine-assisted assembly of Au nanoparticles on Cu nanowires to enhance the electrochemical reduction of CO_2. Angew Chem Int Ed Engl 58:14100–14103

[8] Tang X, Wu Y, Shen Y, Huang Z, Jiang W, Zhao Y, Lv W, Zhu Y (2024) Heterogeneous-structure-based AuNBs@TiO_2 nano-photosensitizers for computed tomography Imaging guided NIR-II photodynamic therapy and cancer metastatic prevention. Adv Healthc Mater 13:2304209

[9] Stoia D, Fazio E, Corsaro C, Campu A, Soritau O, Craciun AM, Chereches G, Focsan M, Neri G, Piperno A (2025) A Graphene–Poly(methacrylic acid)–Gold bipyramid hybrid Plasmonic nanocomposite for in vitro bioimaging and photothermal therapy. J Mater Chem B 13:4433–4446

[10] Jambhulkar S, Ravichandran D, Zhu Y, Thippanna V, Ramanathan A, Patil D, Thummalapalli SV, Sundaravadivelan B, Sun A, Xu W, Yang S, Kannan AM, Golan Y, Lancaster J, Chen L, Joyee EB, Song K (2024) Nanoparticle assembly: from self-organization to controlled micropatterning for enhanced functionalities. Small 20:2306394

[11] Nie Z, Petukhova A, Kumacheva E (2010) Properties and emerging applications of self-assembled structures made from inorganic nanoparticles. Nat Nanotechnol 5:15–25
[12] Jiang N, Zhuo X, Wang J (2018) Active plasmonics: principles, structures, and applications. Chem Rev 118:3054–3099
[13] Middleton AA, Wingreen NS (1993) Collective transport in arrays of small metallic dots. Phys Rev Lett 71:3198–3201
[14] Creighton JA, Blatchford CG, Albrecht MG (1979) Plasma resonance enhancement of Raman scattering by pyridine adsorbed on silver or gold sol particles of size comparable to the excitation wavelength. J Chem Soc Faraday Trans 2 75:790–798
[15] Maier SA, Kik PG, Atwater HA, Meltzer S, Harel E, Koel BE, Requicha AAG (2003) Local detection of electromagnetic energy transport below the diffraction limit in metal nanoparticle plasmon waveguides. Nat Mater 2:229–232
[16] Langer J, Jimenez de Aberasturi D, Aizpurua J, Alvarez-Puebla RA, Auguié B, Baumberg JJ, Bazan GC, Bell SEJ, Boisen A, Brolo AG, Choo J, Cialla-May D, Deckert V, Fabris L, Faulds K, García de Abajo FJ, Goodacre R, Graham D, Haes AJ, Haynes CL, Huck C, Itoh T, Käll M, Kneipp J, Kotov NA, Kuang H, Le Ru EC, Lee HK, Li JF, Ling XY, Maier SA, Mayerhöfer T, Moskovits M, Murakoshi K, Nam JM, Nie S, Ozaki Y, Pastoriza-Santos I, Perez-Juste J, Popp J, Pucci A, Reich S, Ren B, Schatz GC, Shegai T, Schlücker S, Tay LL, Thomas KG, Tian ZQ, Van Duyne RP, Vo-Dinh T, Wang Y, Willets KA, Xu C, Xu H, Xu Y, Yamamoto YS, Zhao B, Liz-Marzán LM (2020) Present and future of surface-enhanced Raman scattering. ACS Nano 14:28–117
[17] Yin Z, Zhang W, Fu Q, Yue H, Wei W, Tang P, Li WJ, Li WZ, Lin L, Ma G, Ma D (2014) Construction of stable chainlike Au nanostructures via silica coating and exploration for potential photothermal therapy. Small 10:3619–3624
[18] Zhong Y, Moore TC, Dwyer T, Butrum-Griffith A, Allen VR, Chen J, Wang Y, Cheng F, Glotzer SC, Ye X (2024) Engineering and direct imaging of nanocube self-assembly pathways. Nat Chem Eng 1:532–541
[19] Wang Y, Chen J, Li R, Götz A, Drobek D, Przybilla T, Hübner S, Pelz P, Yang L, Apeleo Zubiri B, Spiecker E, Engel M, Ye X (2023) Controlled self-assembly of gold nanotetrahedra into quasicrystals and complex periodic supracrystals. J Am Chem Soc 145:17902–17911
[20] Wang Y, Chen J, Zhong Y, Jeong S, Li R, Ye X (2022) Structural diversity in dimension-controlled assemblies of tetrahedral gold nanocrystals. J Am Chem Soc 144:13538–13546
[21] Shibu Joseph ST, Ipe BI, Pramod P, Thomas KG (2006) Gold nanorods to nanochains: mechanistic investigations on their longitudinal assembly using α,ω-alkanedithiols and interplasmon coupling. J Phys Chem B 110:150–157
[22] Wang Y, DePrince AE III, Gray SK, Lin X-M, Pelton M (2010) Solvent-mediated end-to-end assembly of gold nanorods. J Phys Chem Lett 1:2692–2698
[23] Jain T, Westerlund F, Johnson E, Moth-Poulsen K, Bjørnholm T (2009) Self-assembled nanogaps via seed-mediated growth of end-to-end linked gold nanorods. ACS Nano 3:828–834
[24] Yun Q, Ge Y, Huang B, Wa Q, Zhang H (2023) Ligand-assisted phase engineering of nanomaterials. Acc Chem Res 56:1780–1790
[25] Selvakannan PR, Dumas E, Dumur F, Péchoux C, Beaunier P, Etcheberry A, Sécheresse F, Remita H, Mayer CR (2010) Coordination chemistry approach for the end-to-end assembly of gold nanorods. J Colloid Interface Sci 349:93–97
[26] Walter MV, Cheval N, Liszka O, Malkoch M, Fahmi A (2012) Hybrid one-dimensional nanostructures: one-pot preparation of nanoparticle chains via directed self-assembly of in situ synthesized discrete Au nanoparticles. Langmuir 28:5947–5955
[27] Duan H, Jia Z, Liaqat M, Mellor MD, Tan H, Nieh M-P, Lin Y, Link S, Landes CF, He J (2023) Site-specific chemistry on gold nanorods: curvature-guided surface dewetting and supracolloidal polymerization. ACS Nano 17:12788–12797
[28] Young KL, Jones MR, Zhang J, Macfarlane RJ, Esquivel-Sirvent R, Nap RJ, Wu JS, Schatz GC, Lee B, Mirkin CA (2012) Assembly of reconfigurable one-dimensional colloidal superlattices due to a synergy of fundamental nanoscale forces. Proc Natl Acad Sci U S A 109:2240–2245
[29] Hüsken N, Taylor RW, Zigah D, Taveau J-C, Lambert O, Scherman OA, Baumberg JJ, Kuhn A (2013) Electrokinetic assembly of one-dimensional nanoparticle chains with Cucurbit[7]uril controlled subnanometer junctions. Nano Lett 13:6016–6022
[30] Wang H, Li H, Gu P, Huang C, Chen S, Hu C, Lee E, Xu J, Zhu J (2023) Electric, magnetic, and shear field-directed assembly of inorganic nanoparticles. Nanoscale 15:2018–2035
[31] Lim JM, Ashar Naveed M, Wang Y, Saraf RF (2025) Kinetics of ion-mediated directed self-assembly of one-dimensional chains of metal nanoparticles in solution. Nanoscale 17:5012–5020
[32] Li Z, Fan Q, Yin Y (2022) Colloidal self-assembly approaches to smart nanostructured materials. Chem Rev 122:4976–5067
[33] Ding WK, Xia Y, Song HY, Li TT, Yang D, Dong AG (2024) Macroscopic superlattice membranes

self-assembled from Gold nanobipyramids with precisely tunable tip arrangements for SERS. Angew Chem Int Ed 63:e202401945

[34] Carone A, Emilsson S, Mariani P, Désert A, Parola S (2023) Gold nanoparticle shape dependence of colloidal stability domains. Nanoscale Adv 5:2017–2026

[35] Severoni E, Maniappan S, Liz-Marzán LM, Kumar J, García de Abajo FJ, Galantini L (2020) Plasmon-enhanced optical chirality through hotspot formation in surfactant-directed self-assembly of Gold nanorods. ACS Nano 14:16712–16722

[36] Chen C, Zheng L, Guo F, Fang Z, Qi L (2021) Programmable self-assembly of Gold nanoarrows via regioselective adsorption. Research 2021:9793074

[37] Hemant RA, Sharma P, Shanavas A, Neelakandan PP (2024) BODIPY directed one-dimensional self-assembly of gold nanorods. Nanoscale 16:12127–12133

[38] Yoon S, Kim MJ, Kim Y, Kim C, Lee B, Chang JH, Soegijopranoto JK, Bae WK, Zaidi SFA, Lee JH (2025) Controlled self-assembly of Silica-coated nanocrystal networks through ligand-depletion-induced gelation. Inorg Chem 64:22842–22851

[39] Chow TH, Li N, Bai X, Zhuo X, Shao L, Wang J (2019) Gold nanobipyramids: an emerging and versatile type of plasmonic nanoparticles. Acc Chem Res 52:2136–2146

[40] Sánchez-Iglesias A, Winckelmans N, Altantzis T, Bals S, Grzelczak M, Liz-Marzán LM (2017) High-yield seeded growth of monodisperse pentatwinned Gold nanoparticles through thermally induced seed twinning. J Am Chem Soc 139:107–110

[41] Li Z, Lim Y, Tanriover I, Zhou W, Li Y, Zhang Y, Aydin K, Glotzer SC, Mirkin CA (2024) DNA-mediated assembly of Au bipyramids into anisotropic light emitting kagome superlattices. Sci Adv 10:eadp3756

[42] Hemant SD, Mandal D, Neelakandan PP (2025) Chromophore driven assembly of gold nanobipyramids for plasmonic and photothermal enhancement toward pyroelectric energy harvesting. Nano Lett 25:15224–15230

[43] Amin MU, Fang J (2022) Self-assembled gold nano-bipyramids for solution-based surface-enhanced Raman spectroscopy detection. ACS Appl Nano Mater 5:10421–10430

[44] Meena SK, Leroux F, Baldeck P, Andraud C, Garavelli M, Parola S, Sulpizi M, Rivalta I (2021) On the origin of controlled anisotropic growth of monodisperse gold nanobipyramids. Nanoscale 13:15292–15300

[45] Sprague-Klein EA, Ho-Wu R, Nguyen D, Coste SC, Wu Y, McMahon JJ, Seideman T, Schatz GC, Van Duyne RP (2021) Modulating the electron affinity of small bipyridyl molecules on single gold nanoparticles for plasmon-driven electron transfer. J Phys Chem C 125:22142–22153

[46] Li JF, Zhang YJ, Rudnev AV, Anema JR, Li SB, Hong WJ, Rajapandiyan P, Lipkowski J, Wandlowski T, Tian ZQ (2015) Electrochemical shell-isolated nanoparticle-enhanced Raman spectroscopy: correlating structural information and adsorption processes of pyridine at the Au(hkl) single crystal/solution interface. J Am Chem Soc 137:2400–2408

[47] Jain PK, Lee KS, El-Sayed IH, El-Sayed MA (2006) Calculated absorption and scattering properties of gold nanoparticles of different size, shape, and composition. J Phys Chem B 110:7238–7248

Supporting Information

CTAB–4,4′-bipyridine Interface-Mediated Self-Assembly of Gold Nanobipyramids into Stable Plasmonic Chains

Lan Chen[1], Xi-Hao Zhang[1], Hironori Ito[2], Tian-Song Deng[1,*]

[1]School of Electronics and Information Engineering, Hangzhou Dianzi University, Hangzhou, 310018, P. R. China

[2]Integrated Graduate School of Medicine, Engineering, and Agricultural Sciences, University of Yamanashi, 4-3-11, Takeda, Kofu, Yamanashi, 400-8510, Japan

[*]Corresponding author. E-mail: dengts@pku.edu.cn

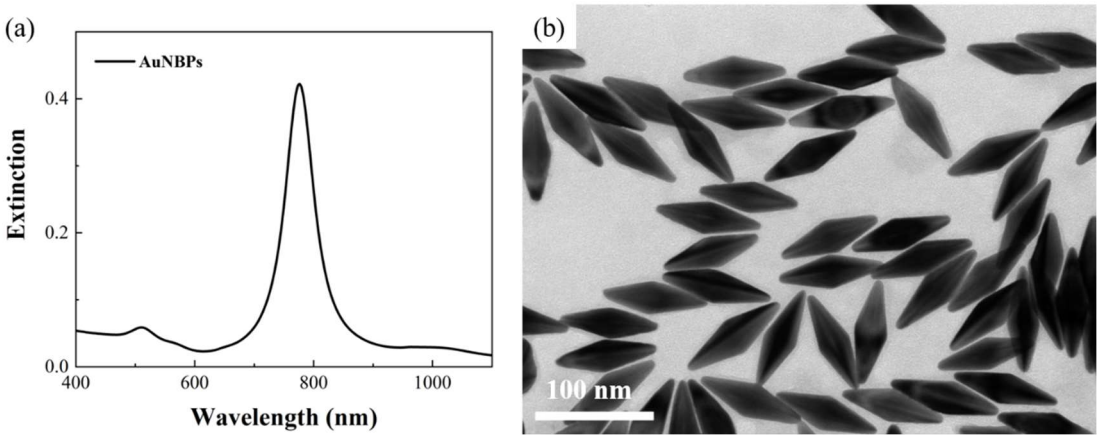

Figure S1. UV–vis–NIR spectrum (a) and TEM image (b) of the AuNBPs.

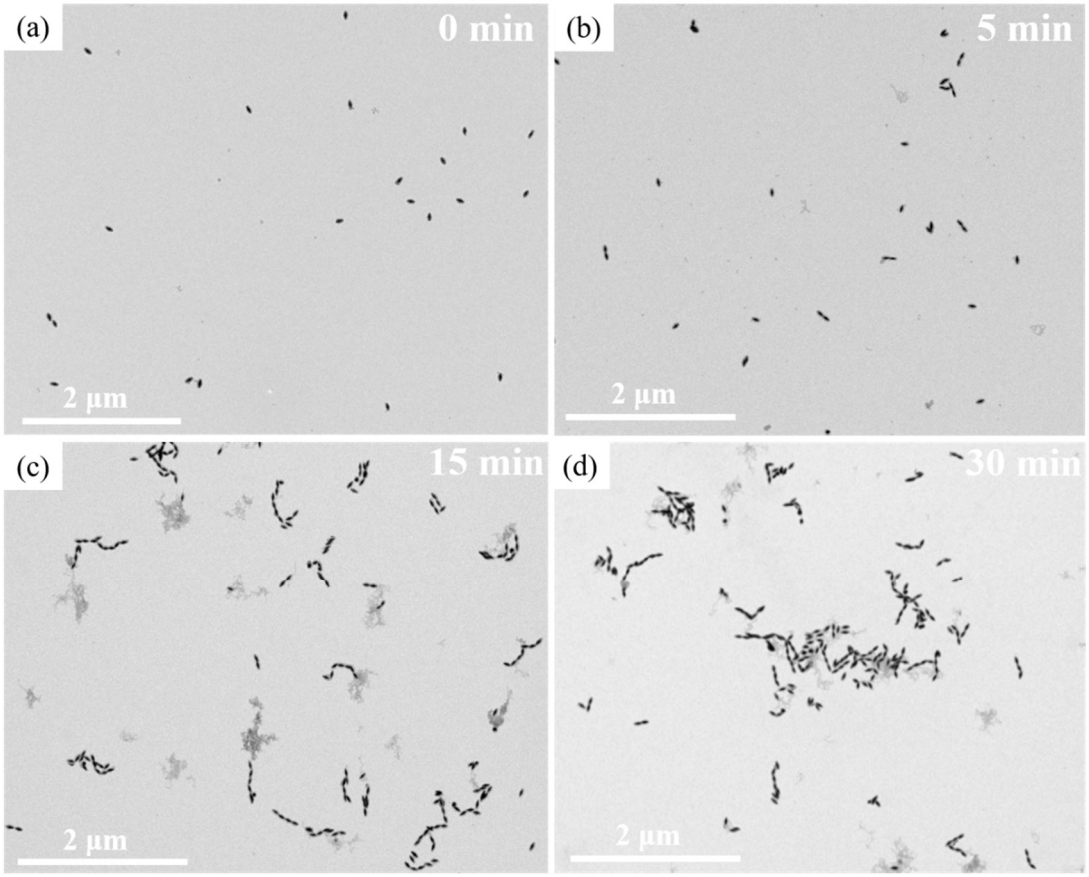

Figure S2. TEM images of SiO_2-coated assemblies after (a) 0 min, (b) 5 min, (c) 15 min, and (d) 30 min assembly under CTAB (10 µM) and 4,4′-bipyridine (1 mM).

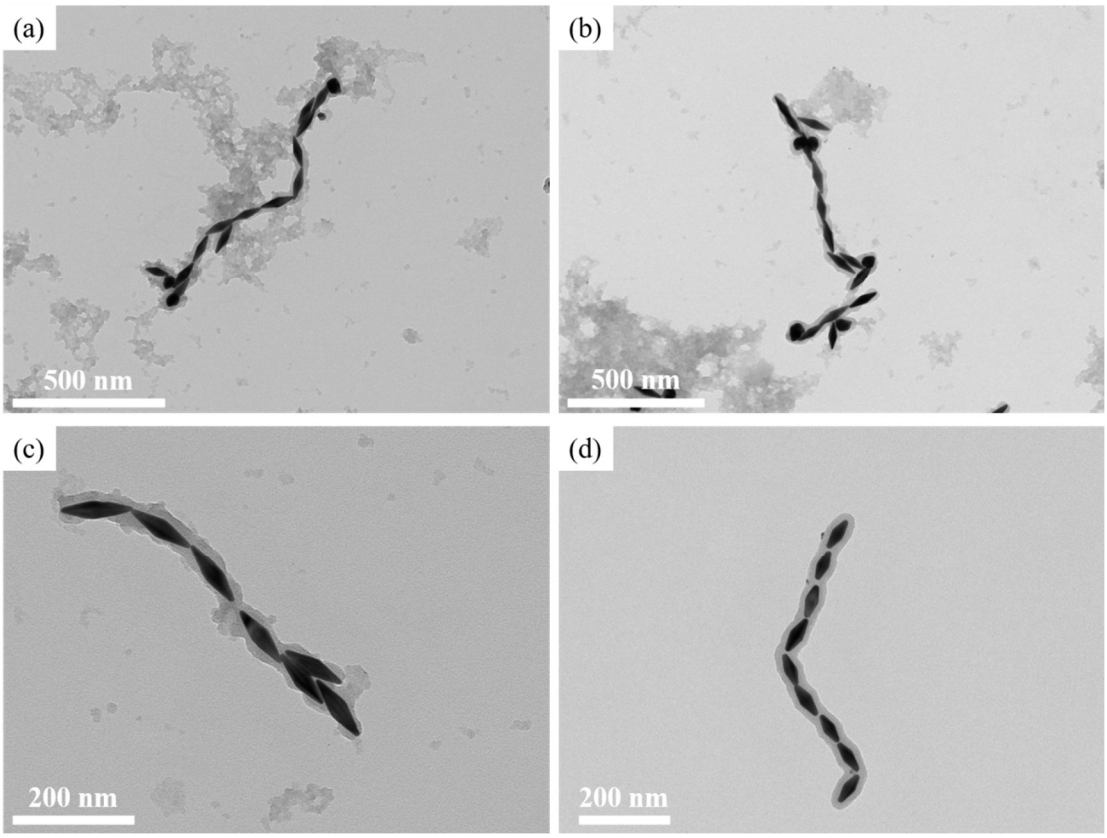

Figure S3. (a–d) TEM images of long chains of assembled AuNBPs with different morphologies.

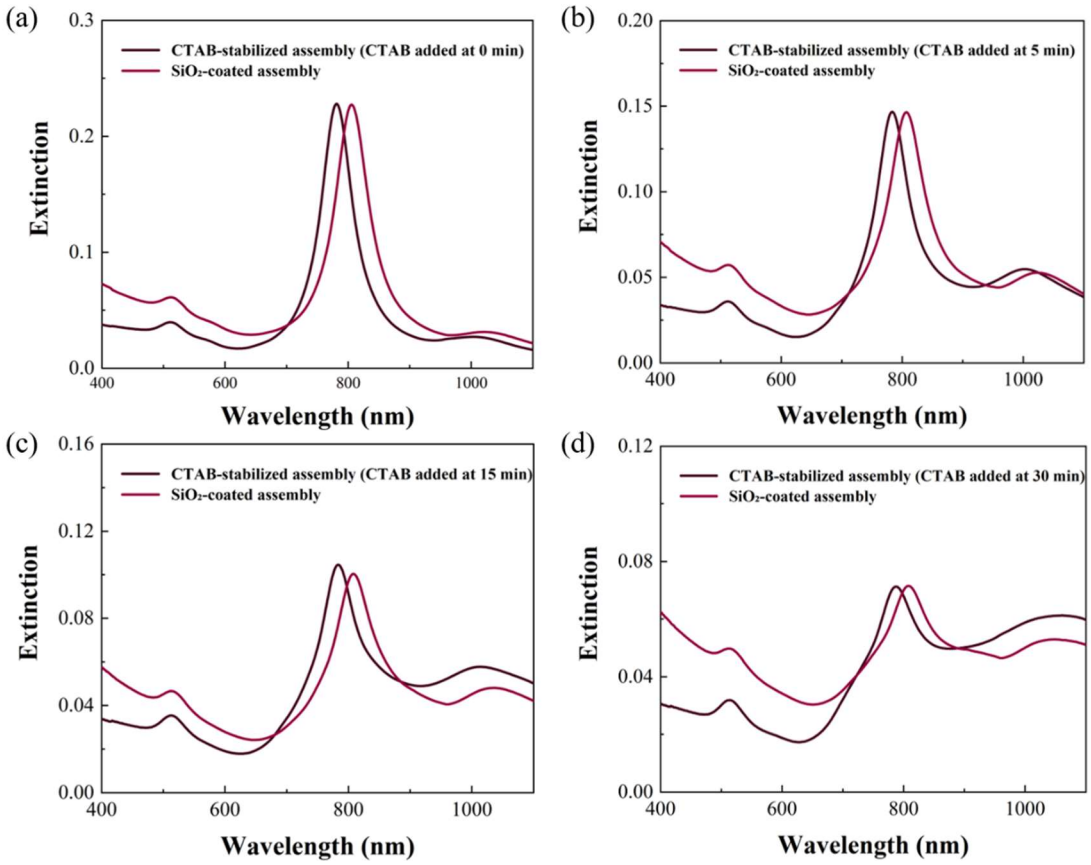

Figure S4. UV–vis–NIR spectra of AuNBPs assemblies arrested by CTAB addition at different assembly time points and after subsequent SiO_2 encapsulation, demonstrating preservation of the longitudinal LSPR features.

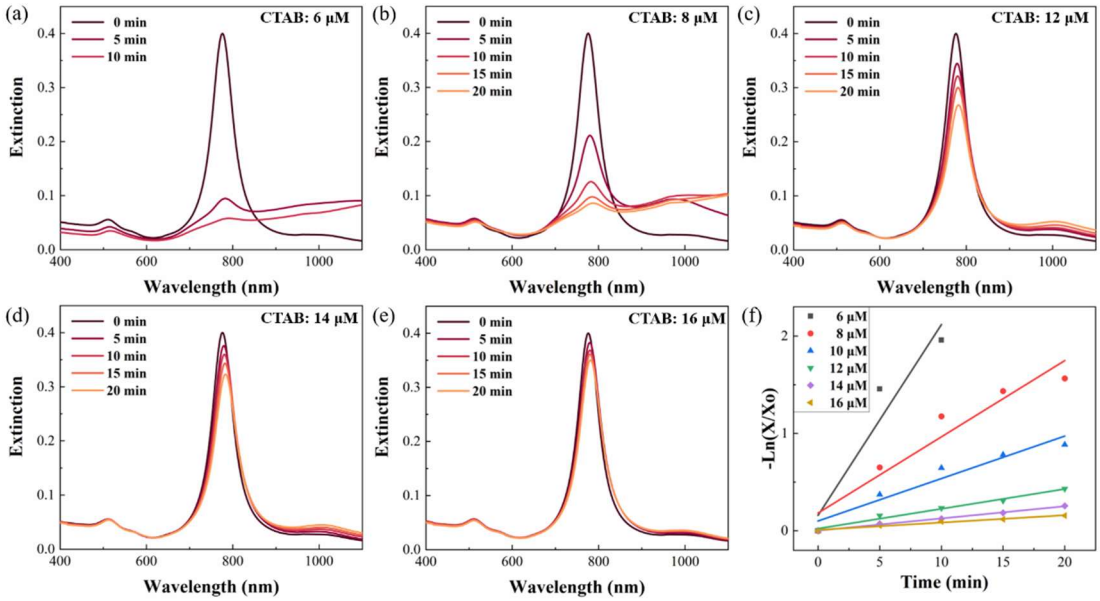

Figure S5. (a–e) Time-dependent UV–vis–NIR spectrum of assembly solutions at different CTAB concentrations with fixed 4,4′-bipyridine (1 mM); (f) Corresponding kinetic scatter plots of the assembly process.

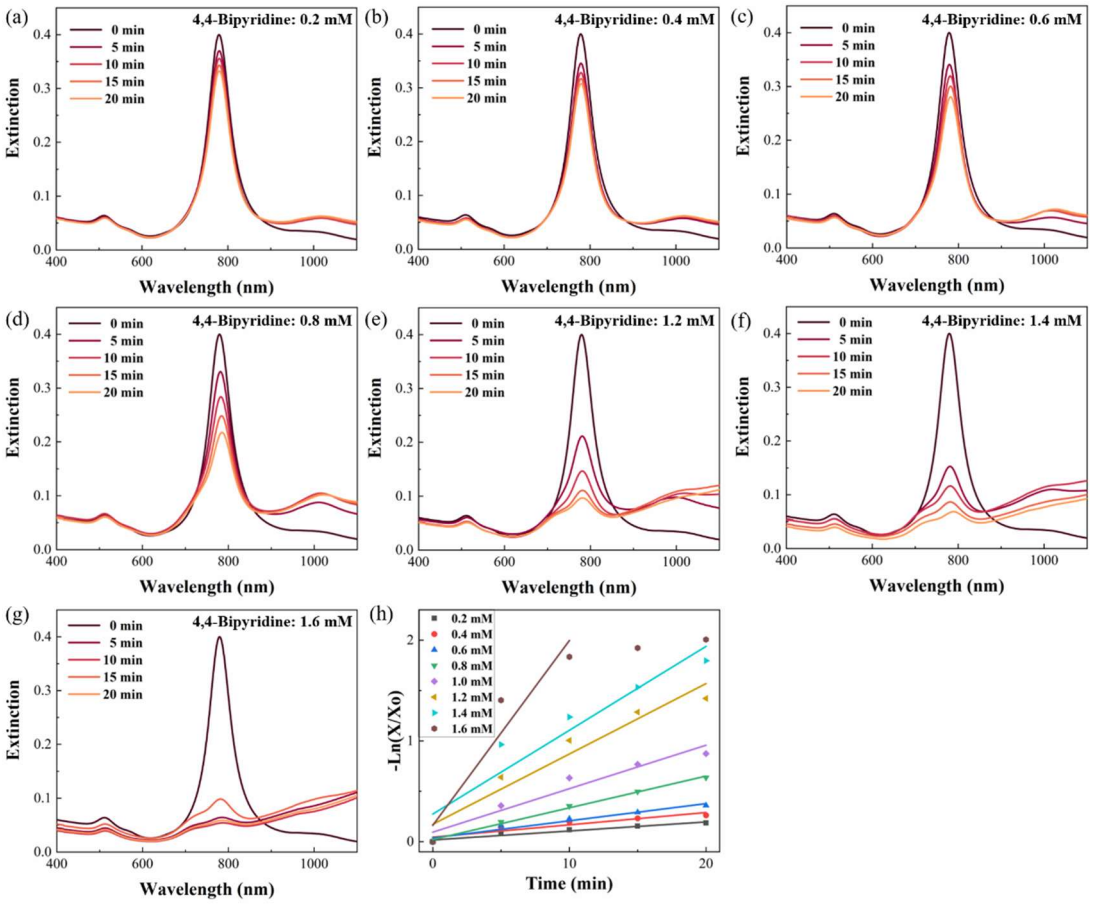

Figure S6. (a–g) Time-dependent UV–vis–NIR spectra of assembly solutions at different 4,4′-bipyridine concentrations with fixed CTAB concentration (10 μM); (h) Corresponding kinetic scatter plots of the assembly process.

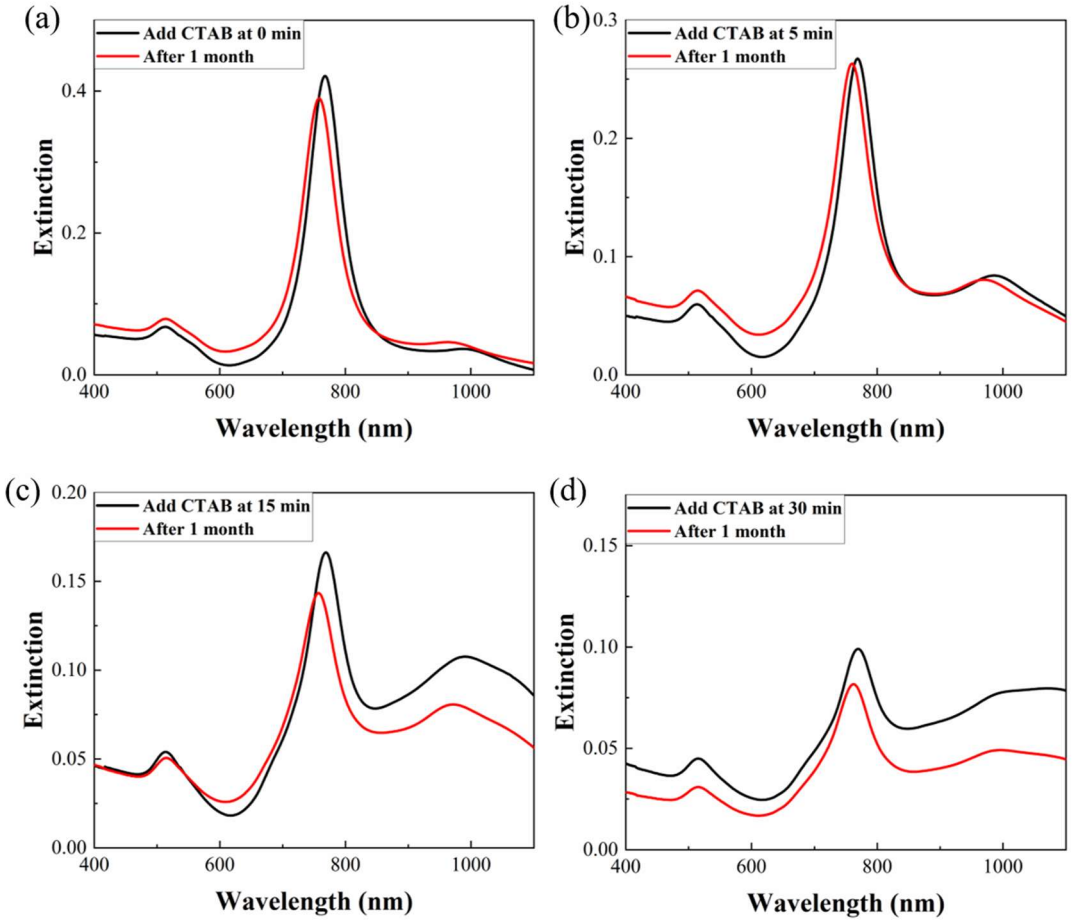

Figure S7. Stability test of AuNBPs assembly solutions after termination by CTAB addition at different time points under CTAB (10 μM) and 4,4′-bipyridine (1 mM): (a–d) UV–vis–NIR spectra recorded immediately after termination and after one month. Minor blue shifts and intensity decreases are observed over time, while no progressive spectral evolution or features associated with further assembly are detected.

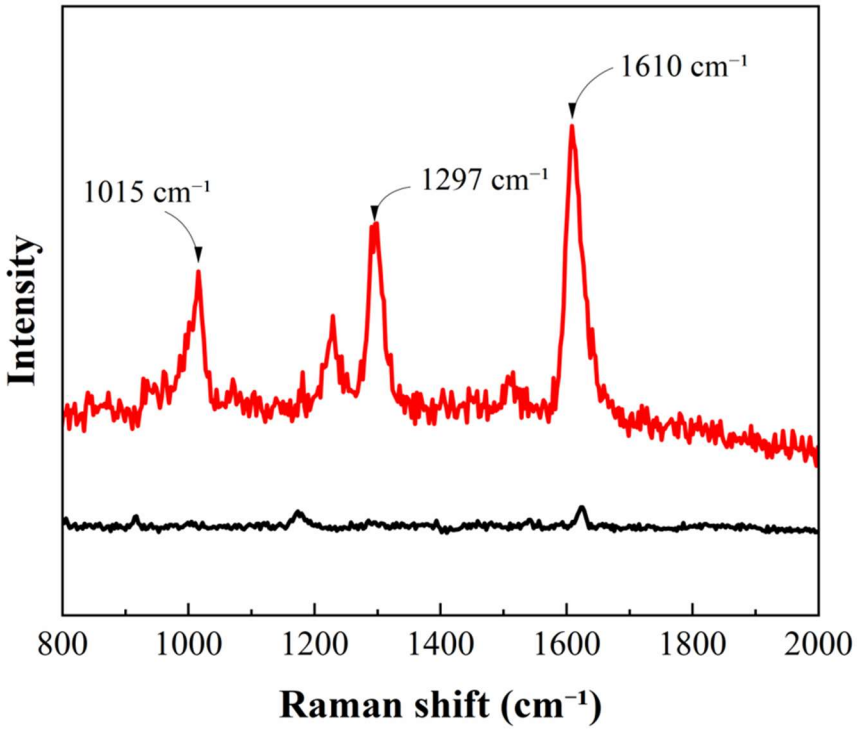

Figure S8. Raman spectra comparison between AuNBPs assembled for 15 min under CTAB (10 μM) and 4,4′-bipyridine (1 mM) and pure 4,4′-bipyridine (1 mM).

FDTD simulation models and geometric definitions

The FDTD simulation framework and general numerical settings follow the methodology described in Section 4.7 of the main text. To facilitate reproducibility and clarify the construction of the simulation geometries, additional details on the assembly models and their geometric definitions are provided here.

Two representative classes of AuNBPs assembly models were constructed for the FDTD simulations, based on the dominant structural motifs observed in TEM images. The first class corresponds to idealized end-to-end assemblies, in which individual AuNBPs were arranged in a tip-to-tip configuration along a common longitudinal axis. In these models, the particles were aligned coaxially with a fixed interparticle separation of 1 nm, chosen as a representative nanoscale spacing consistent with experimentally observed interparticle separations in TEM images. Chain lengths ranging from n = 2 to 6 were considered.

For the idealized tip-to-tip chain models, the degree of bending was quantitatively defined by the angle between the longitudinal axes of two adjacent AuNBPs. A bending angle of 0° corresponds to a perfectly linear chain, while larger angles indicate increasing curvature. To systematically examine the influence of chain curvature on the optical response, bending angles of 30°, 60°, 90°, and 120° were investigated, as schematically indicated by the arrows in Figure 5 and Figures S9–S12. These discrete angles span the range of chain curvature observed experimentally while maintaining well-defined and reproducible geometries.

The second class of models represents laterally staggered and partially overlapped assemblies, which are frequently observed in the experimental samples. In these configurations, adjacent AuNBPs were laterally displaced to introduce a controlled overlap between the slanted facets, while maintaining a fixed minimum interparticle separation of 1 nm at the nearest contact points. In the main text (Figure 6), the lateral overlap was fixed at 11.11% and the chain length was varied from n = 2 to 5 to examine chain-length effects under a representative staggered configuration. The influence of increasing overlap was further explored in the Supporting Information, where overlap degrees of 50% and 100% were considered (Figures S13 and S14).

For all simulated configurations, the AuNBPs were modeled as back-to-back bicones using the average particle dimensions extracted from TEM analysis. The surrounding media and excitation conditions were identical to those described in Section 4.7 of the main text.

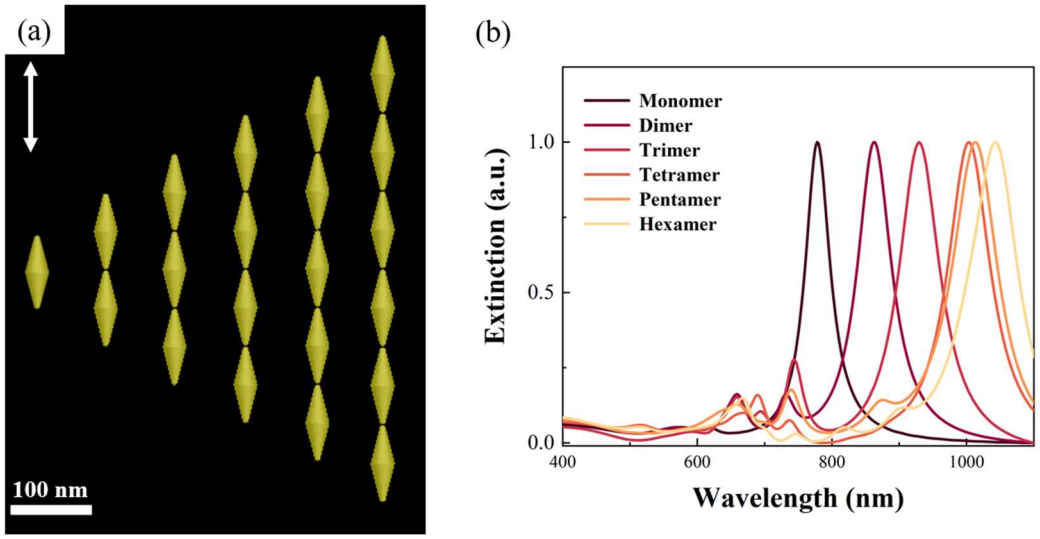

Figure S9. (a) Geometric models and (b) corresponding FDTD-simulated extinction spectrum of AuNBPs assemblies with different chain lengths (n = 1–6) at a bending angle of 0°.

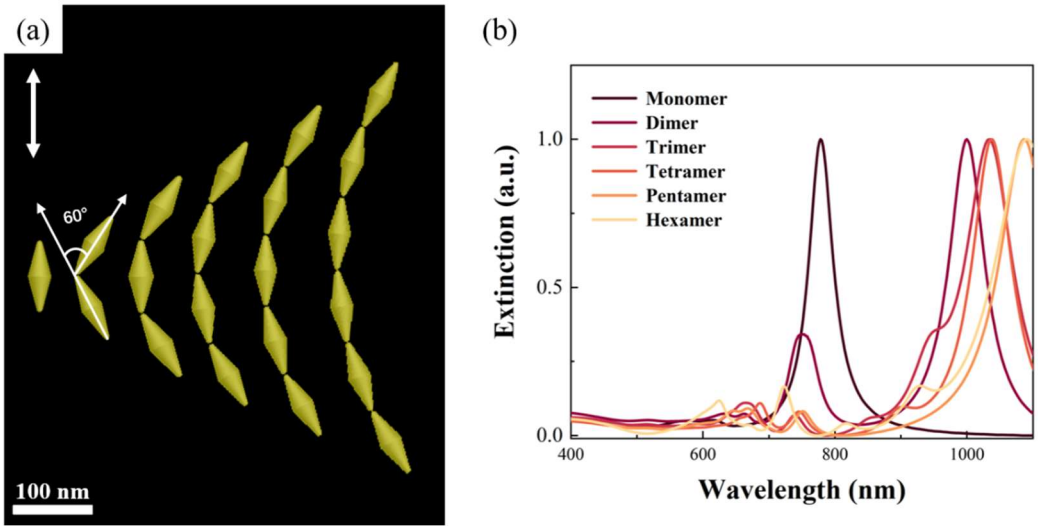

Figure S10. (a) Geometric models and (b) corresponding FDTD-simulated extinction spectra of AuNBPs assemblies with different chain lengths (n = 1–6) at a bending angle of 60°.

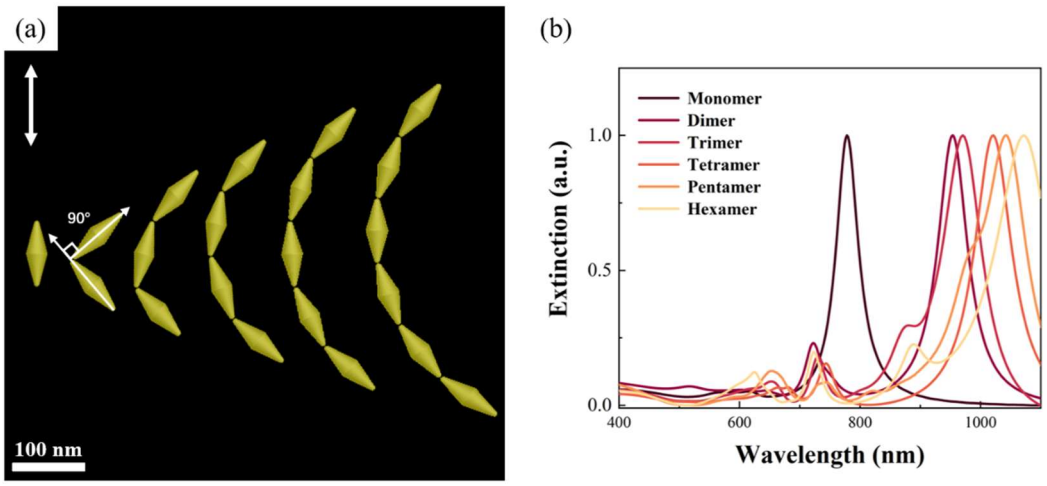

Figure S11. (a) Geometric models and (b) corresponding FDTD-simulated extinction spectra of AuNBPs assemblies with different chain lengths (n = 1–6) at a bending angle of 90°.

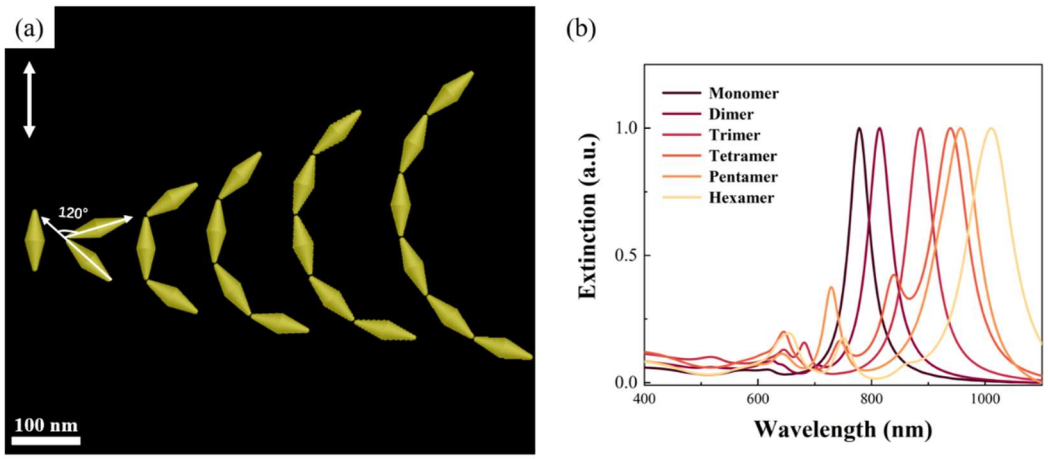

Figure S12. (a) Geometric models and (b) corresponding FDTD-simulated extinction spectra of AuNBPs assemblies with different chain lengths (n = 1–6) at a bending angle of 120°.

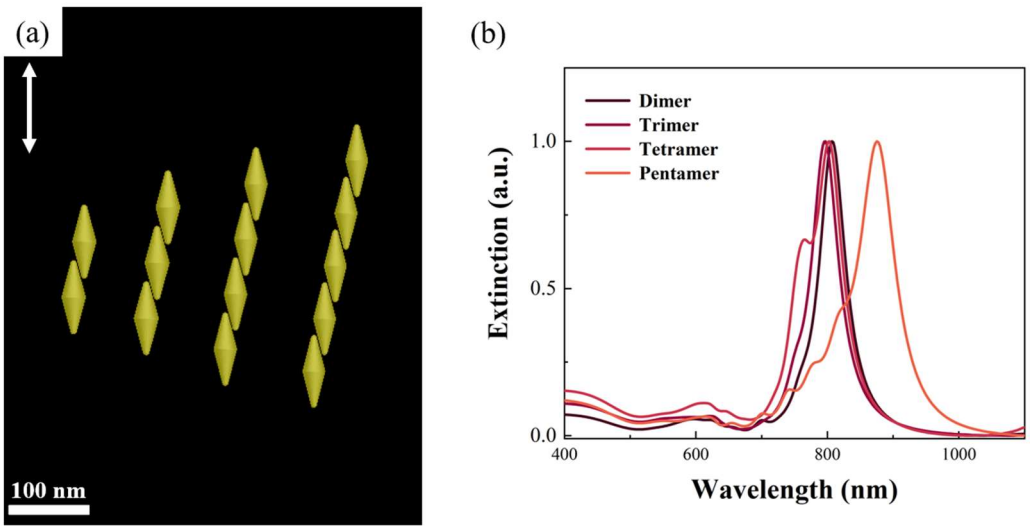

Figure S13. (a) Geometric models and (b) corresponding FDTD-simulated extinction spectra of AuNBPs assemblies with different chain lengths (n = 2–5) at 50.0% lateral overlap.

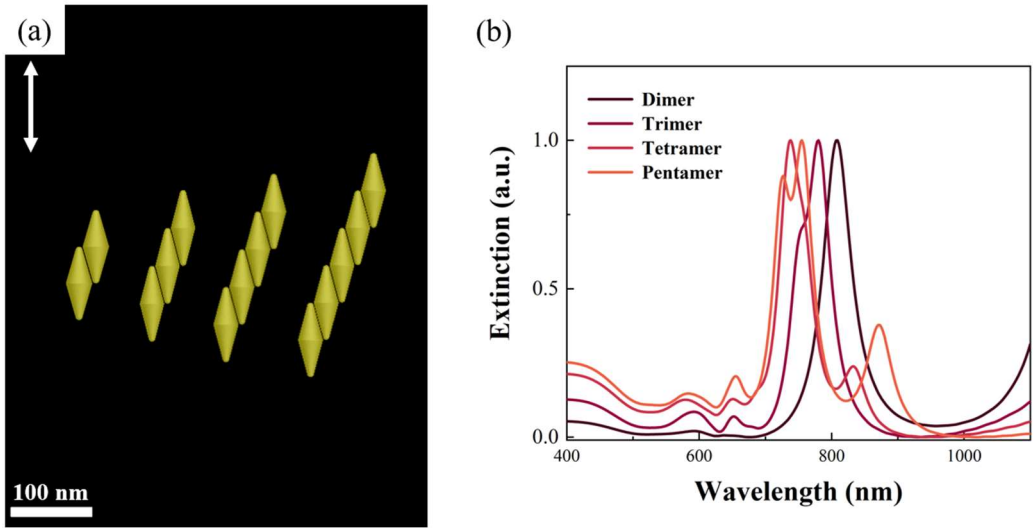

Figure S14. (a) Geometric models and (b) corresponding FDTD-simulated extinction spectra of AuNBPs assemblies with different chain lengths (n = 2–5) at 100.0% lateral overlap.